Dewetting dynamics of silicon-on-insulator thin films

F. Cheynis,* E. Bussmann,† F. Leroy, T. Passanante, and P. Müller

Centre Interdisciplinaire de Nanoscience de Marseille (CINaM), UPR CNRS 3118, Aix-Marseille Université, Case 913, Campus de Luminy, FR-13288 Marseille Cedex, France

(Received 3 November 2011; published 20 December 2011)

Using low-energy electron microscopy (LEEM), we have measured, in real time, the dewetting of single-crystal Si(001) thin films on amorphous silicon dioxide substrates, which transforms the two-dimensional (2D) thin film into three-dimensional (3D) compact Si nanocrystals. The dewetting scenario has been reported by Bussmann *et al.* [New J. Phys. **13**, 043017 (2011)]. Analytic 2D and 3D models based on simple approximate geometries of the dewetting front have been developed to analyze LEEM measurements. They enable us to estimate the driving force for dewetting $E_s \sim 14$ eV/nm^2. Starting from a Si-film thickness dependent *effective* dewetting activation barrier, a single Si(001) surface self-diffusion energy of $E_a = 2.0 \pm 0.2$ eV is derived. First nanoisland-formation dynamics measurements are discussed. Finally, grazing incidence small-angle x-ray scattering (GISAXS) is used to characterize the structure and the morphology of the Si nanocrystals created by the dewetting process.

DOI: 10.1103/PhysRevB.84.245439 PACS number(s): 68.35.Fx, 68.35.Md, 68.37.Nq

I. INTRODUCTION

Solid thin films with thickness of a few nanometers are crucial elements in numerous technologies, e.g., microelectronics and catalysis. In many systems, the flat two-dimensional (2D) film is a nonequilibrium configuration, so that the film may *dewet* upon thermal treatments to form compact three-dimensional (3D) structures.[1–5] Silicon-on-insulator (SOI) is an example of a metastable film that undergoes a dewetting instability when annealed.[6–11] This key building block for the next generation CMOS microelectronics consists of a single-crystalline Si thin film, in our case Si(001), on an amorphous silicon dioxide substrate.

Although many *ex situ* analyses of the morphology of dewetted SOI films are already available,[6–18] a detailed *in situ* characterization of the dynamic evolution of the SOI dewetting process has only been reported recently.[19] For this purpose, we have used low-energy electron microscopy (LEEM). This technique gives simultaneously access, in *real time*, to the micrometric lateral scale of the dewetting area and the atomic vertical scale. In our previous work, we have confirmed the following dewetting scenario: (i) the heterogeneous nucleation at randomly distributed defects and growth of voids surrounded by (ii) a thickening rim, (iii) the formation of Si fingers, and (iv) the breakdown of Si fingers into 3D nanoislands. This paper also shows that Si dewetting from a SiO_2 substrate is mediated by surface diffusion and driven by surface-free-energy minimization.

This paper extends our previous paper[19] in many respects. In Sec. II, we clearly show the effect of the surface preparation on the dewetting morphologies, possibly explaining the different void-growth behaviors reported in the literature. The different dewetting stages are then reviewed and new analysis is brought forward: the 2D analytic model for the thickening rim velocity given in Ref. 19 is described in more detail and further analytic solutions are discussed relative to existing theoretical predictions (Sec. III B). Section IV compares the observed rim instability with Ref. 20, which interpreted this phenomenon in terms of a Rayleigh-Plateau instability. In Sec. V, a 3D model for the Si finger formation is introduced, enabling us to determine a geometry-independent activation energy of 2.0 ± 0.2 eV, in quantitative agreement with the value of 2.3 ± 0.1 eV for Si(001) surface diffusion obtained in Ref. 21. First, experimental results on the nanoisland formation dynamics using both LEEM and grazing incidence small-angle x-ray scattering (GISAXS) are described in Sec. VI. Finally, in Sec. VII, we discuss several potential additional effects that could play a role in dewetting.

II. EXPERIMENT

A. Methods and materials

Experimental investigations were done on silicon-on-insulator (SOI) thin films fabricated by means of the Smart Cut© process at CEA-LETI (Grenoble, France). SOI samples are a single-crystal Si(001) film bonded onto a ∼140-nm-thick oxide layer on a Si(001) substrate.

The experiments are performed with an ELMITEC LEEM III microscope at pressures $<10^{-9}$ Torr (base pressure $<2 \times 10^{-10}$ Torr). SOI samples with different Si thicknesses (6, 11, 14, and 22 ± 2 nm) are first prepared *ex situ* by repeated cycles of chemical oxidation (H_2SO_4:H_2O_2, 3:1 by volume), and stripping of the oxide with HF acid. In the final step, a protective oxide layer (∼1–2 nm thick) is formed in a HCl:H_2O_2:H_2O (3:1:1 by volume) solution. After introduction in the ultrahigh vacuum (UHV) setup, samples are degassed overnight at 500 °C. Prior to dewetting, the oxide layer is desorbed by annealing at ∼700 °C. The reaction $Si + SiO_2 \rightarrow 2SiO$ with SiO molecules desorbing into vacuum is indeed active at temperatures >700 °C.[22] Subsequent low-energy electron diffraction (LEED) measurements [Fig. 1(a)] show that the surface has 1/2-order spots associated with the (2×1) and (1×2) reconstructions characteristic of a clean Si(001) surface under UHV conditions.

In dewetting experiments, the sample is annealed at a fixed temperature ($T > 700$ °C), while a sequence of LEEM images is recorded at a fixed rate to create a movie of the dewetting process. The images are typically recorded in dark-field mode using electrons from one of the 1/2-order LEED spots associated with the surface reconstruction. Adjacent Si(001) terraces have orthogonal reconstructions [(2×1)

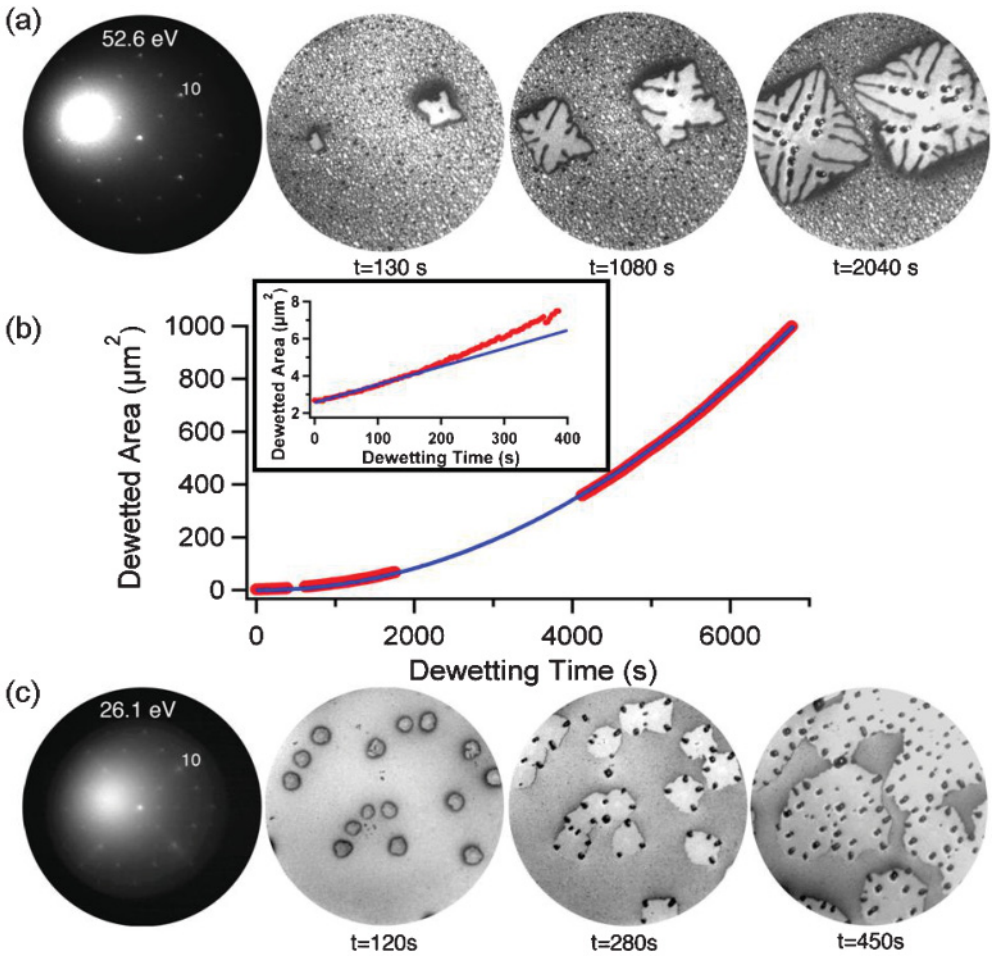

FIG. 1. (Color online) (a) LEEM images of SOI dewetting (SOI 22 ± 2 nm thick, $T = 870\ ^{\circ}$C, $E_{e^-} = 7.8$ eV) of a clean surface showing strong $1/2$-order LEED spots. Bright-dark speckling is due to the 2×1 Si surface (dark-field conditions). Void nucleation starts on morphological defects at $t = 0$ s. The images have been taken at $t = 130$ s (square-void opening), then $t = 1080$ s (instability of the side of the square voids), and $t = 2040$ s (finger growth and nanoisland formation in organized rows). (b) Typical time evolution of a given dewetting void imaged in (a). Blue solid lines show the linear (inset) and quadratic time evolution of a dewetted area. (c) LEEM sequence of a surface prepared inadequately [i.e., not showing strong (2×1) and (1×2) LEED spots]. Images have been obtained, respectively, at $t = 120$, 280, and 450 s. For all images, field of view (FOV) is 25 μm.

versus (1×2)] so that they appear alternately bright and dark according to the reconstruction orientation [Fig. 1(a)]. This contrast gives us direct access to the local vertical atomic-scale structure of the surface, so that we can observe in *real time* the motion of individual steps. The contrast also gives direct insight into nucleation processes on facetted 3D structures during dewetting. In addition to LEEM measurements, *ex situ* noncontact atomic force microscopy (AFM) is used to characterize the sample topography (PSIA-XE 100).

B. Dewetting sequence and surface preparation

Figure 1(a) shows a LEEM image sequence of the dewetting of a SOI thin film. The dewetting process is qualitatively identical for Si films 6 to 22 nm thick: (i) square crystallographically oriented voids nucleate heterogeneously at defects in the Si layer, exposing the oxide (which appears bright due to charging effects), (ii) the voids grow spontaneously and give rise to a Si rim at the edge, (iii) the rim undergoes a shape instability to form Si fingers, and (iv) the fingers break apart into Si nanocrystals.[13,15] This dewetting pathway is characteristic of a clean Si(001) surface exhibiting strong (2×1) and (1×2) LEED spots

We observe a different dewetting pathway [Fig. 1(c)] for samples that have been either simply loaded directly in the UHV system, without preparation, or prepared inadequately, e.g., kept in vacuum a long time (>10 h) after decomposition of the chemical oxide prior to dewetting. The sample surfaces show a $c(4 \times 4)$ reconstruction characteristic of a residual C contamination.[23] Figure 1(c) shows a LEEM image sequence of the dewetting of such a contaminated sample in which (i) round voids open heterogeneously in the Si film, (ii) the voids grow without the formation of a 3D Si rim, (iii) the void edges do not exhibit elongated fingers, but facetted compact 3D Si nanocrystals, and (iv) the film edge retracts, leaving isolated nanocrystals on the oxide. The resulting islands are relatively disorganized, compared to those obtained from a clean Si(001) surface. In the literature, results corresponding to both pathways can be found.[8,24]

III. INITIAL STAGES OF DEWETTING

A. Square-void and rim formations

SOI dewetting begins with heterogeneous nucleation of voids with ⟨110⟩-oriented sides. From the LEEM image sequences, it is possible to follow the dewetting phenomenon at the micron scale by measuring the time evolution of individual void areas [Fig. 1(b)]. In the initial stage (i.e., as long as the voids remain square shaped), the dewetted area increases approximately linearly in time. The material (Si) expelled from the void is transferred to a 3D rim.[19] This rim is facetted and a {001} top facet is observed in atomic force microscopy [Fig. 2(b)] and LEEM measurements. In dark-field imaging, rim summits exhibit a dark or bright contrast [Fig. 2(a)]. Additional lateral facets are also expected [e.g., {111} (Refs. 11 and 12)].

In LEEM movies, successive atomic layers added to the rim top facet appear alternately bright and dark, owing to their orthogonal surface reconstructions. As the void grows, the rim thickens *via* the nucleation of new layers on the top {001} facet.

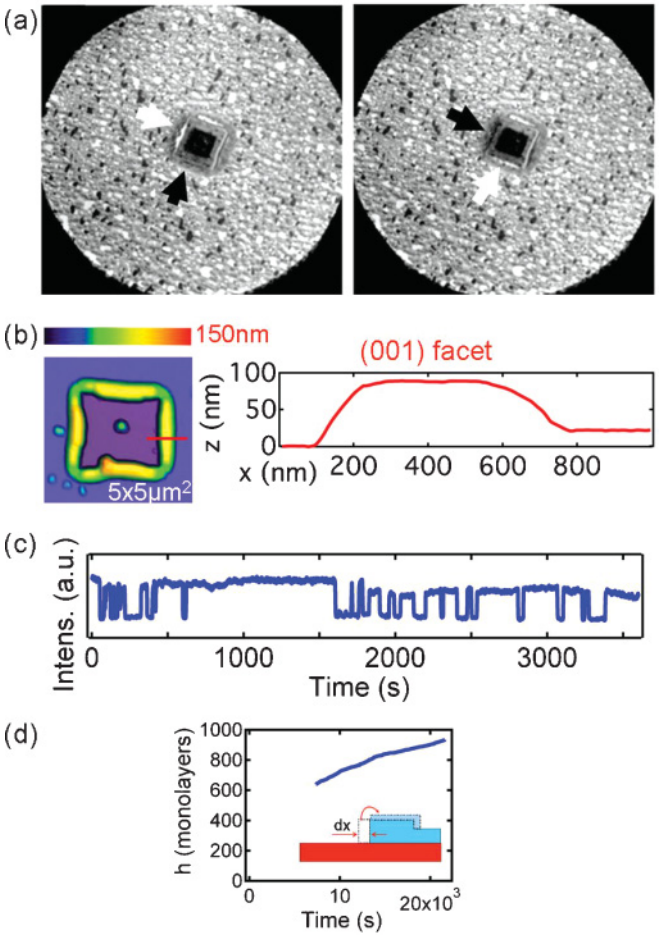

FIG. 2. (Color online) (a) Dark-field LEEM images illustrating the contrast inversion of the two {001} top facets (cf. arrows) due to the nucleation and completion of a new monolayer on each top facet (SOI 22 ± 2 nm thick, $T = 766$ °C, $E_{e^-} = 3.8$ eV, FOV $= 25$ μm). (b) AFM image and profile of a dewetting void and rim. (c) Time evolution of the contrast of a {001} top facet. (d) Average height of the rim versus time.

Figure 2(b) illustrates the contrast change of the {001} top facet during void growth. By recording on each facet the LEEM intensity as a function of time [Fig. 2(c)], the height of the rim as well as the nucleation and growth kinetics are monitored in real time. The rim height versus time is obtained by counting the new layers on the top facet of the rim [Fig. 2(d)]. The height evolution of the rim is limited by the nucleation rate rather than by the layer completion. Once a new layer has nucleated, it spreads and covers the facet much faster than the time between nucleation events. From our measurements, no clear evidence of a height-dependent nucleation barrier, as predicted by Ref. 25, can be found. A detailed study of the nucleation properties on the top facet will be published in a forthcoming paper.

B. Modeling of the rim velocity and determination of the driving force

To model the dewetting dynamics of the Si layer, we have developed a 2D approach describing the experiments shown in Fig. 1(a) and the kinetic Monte Carlo (KMC) simulations reported in Ref. 19. In this analytic model, depicted in Fig. 3, a facetted rim recedes by surface-diffusion-mediated mass transfer from the base of the rim to the top of the rim. The growth and thickening of the rim *via* nucleation on the top facet are also accounted for.

We assume that the rim position $x(t)$ moves with a velocity determined by an Einstein relation $v_{\rm rim} = -MF$, where M is an effective surface-diffusion-based mobility, and F is a thermodynamic driving force.[26] In the model geometry, the driving force per unit length of dewetting front when displaced by a distance δx is $F = -(\gamma_{\rm Si} + \gamma_{\rm int} - \gamma_{\rm Ox}) + 2\gamma_{\rm Si}\delta h/\delta x$. The first term $E_s = \gamma_{\rm Si} + \gamma_{\rm int} - \gamma_{\rm Ox}$ is associated with the decrease of surface and interface free energies due to the void growth and $2\gamma_{\rm Si}\delta h/\delta x$ is associated with the change of height. Since the rim is wide, $E_s \gg 2\gamma_{\rm Si}\delta h/\delta x$ and the driving force per unit length is $\approx -E_s$. Using Morgenstern's method,[27] we determine the mobility of the rim assuming that surface diffusion, across the width w of the rim, is limiting. The number of atoms involved during the rim displacement δx is proportional to the square root of the number of atoms diffusing on the surface of the rim during time t: $N \sim hL\delta x/\Omega \sim \sqrt{n_o t/\tau}$, where L is the (arbitrary) length of the rim, Ω is an atomic volume, and n_o the number of adspecies on the surface. In a diffusion-limited regime, the average time to cross the rim of width w is $\tau \sim w^2/D_s$, where D_s is the diffusion coefficient for adspecies. The number of adspecies on the surface is $n_o \sim wLc/a^2$ with c the adspecies surface fraction and a an atomic distance. We obtain $\delta x^2 = D_{\rm eff} \times t$, where $D_{\rm eff}$ is an effective diffusion coefficient ($D_{\rm eff} = M \times k_B T$). Putting all together, we obtain $M = \Omega^2 D_s c/(a^2 L h^2 w k_B T)$ and $v_{\rm rim} =$

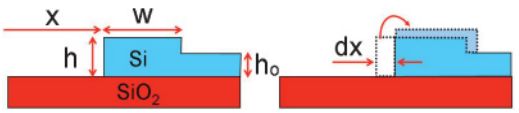

FIG. 3. (Color online) Geometry used to model a 2D rim receding *via* thickening. Owing to thickening, the rim slows down as it moves outward.

TABLE I. Analytic expressions obtained by integration of Eq. (1) for two asymptotic conditions assuming mass conservation ($xh_0 = w\Delta h$). $K = \frac{\Omega^2}{a^2}\frac{D_{s,o}c_0}{k_BT}E_s e^{-E_a/k_BT}$, where h_0 is the initial thickness of the film, h the actual rim thickness, and $\Delta h = h - h_0$ the height excess at the rim.

Geometry assumption	$h = Cst$	$\alpha = \Delta h/w = Cst$
$x(t)$	$x^2 = 2K\frac{\Delta h}{h_0 h^2}t$	$\left(\frac{2}{3}h_0^2 x^{3/2} + \frac{h_0^{3/2}}{\alpha^{1/3}}x^2 + \frac{2}{5}\frac{h_0}{\alpha}x^{5/2}\right) = K\left(\frac{\alpha}{h_0}\right)^{1/2}t$

$-MF = (\Omega^2 D_s c/a^2h^2w)(E_s/k_BT)$ similar to Ref. 25. In the following, we write

$$v_{\rm rim} = \left(\frac{\Omega^2}{h^2 w a^2}\right) D_{s,o}c_o e^{-E_a/k_BT}\left(\frac{E_s}{k_BT}\right), \qquad (1)$$

where $D_{s,o}$ and c_o are the diffusion and the adspecies surface fraction prefactors and $E_a = E_{\rm diff} + E_{\rm form}$ is an activation energy that can be written as the sum of the formation energy ($E_{\rm form}$) and the diffusion barrier ($E_{\rm diff}$) of the diffusing species. Note that the front velocity [Eq. (1)] can be written as a function of the chemical potential at the facetted rim $\mu = E_s/h$ (Ref. 28):

$$v_{\rm rim} = (\Omega/a)^2 D_{s,o}c_o \frac{e^{-E_a/k_BT}}{hw}\left(\frac{\mu}{k_BT}\right). \qquad (2)$$

In general, $h(t)$ and $w(t)$ are required to calculate the velocity of the dewetting front [Eq. (1)]. However, in a few special cases, expressions of $x(t)$ can be obtained by integration of Eq. (1), leading to an area variation $A(t) \propto t^\chi$ with, $\chi = 1$ or $4/5$ for, respectively, a constant rim height h and a constant rim aspect ratio $\alpha = (h - h_0)/w$ (Table I). Note that the exponent $4/5$ found at constant α in the long-time limit is consistent with the exponent found in Refs. 29 and 30, respectively, for a 3D opening void with a contact angle of 90° and for the motion of a straight dewetting front. Both reports use an isotropic diffusion-limited model. To be thorough, Srolovitz and Safran numerically found $\chi = 1/2$ when considering a continuous 2D model[31] and Jiran and Thompson predict a constant edge velocity (i.e., $\chi = 2$) for a dewetting front exhibiting fingers.[1]

From our expression of the rim velocity $v_{\rm rim}$, the SOI dewetting driving force can be determined. Using the measured evolution $h(t)$ [Fig. 2(f)] and assuming mass conservation [$xh_o = w(h - h_o)$], we numerically integrate our expression of $v_{\rm rim}$ and fit it to the void area versus time experiments using E_s as the only fit parameter. The value of the surface self-diffusivity, $D_s c = D_{s,o}c_o e^{-E_a/k_BT}$ at $T \sim 800$ °C is 10^6 nm^2/s.[21] The best fit is obtained for $E_s \sim 14$ eV/nm^2 (~ 2.3 J/m^2) (Fig. 4). For comparison, the value of E_s can be estimated from the literature and our AFM data [$E_s = \gamma_{\rm Si} + \gamma_{\rm Si\text{-}SiO_2} - \gamma_{\rm SiO_2} = \gamma_{\rm Si}(1 + \cos\theta_c)$ where θ_c is the Si-SiO_2 equilibrium contact angle]. From Refs. 32–34, $\gamma_{\rm Si} \sim 5$–9 eV/nm^2 at $T = 830$ °C. Anisotropy of $\gamma_{\rm Si}$ is negligible ($\sim 10\%$).[35] From AFM data, we estimate $\theta_c \sim 50°$–$80°$. Using these numbers, we estimate that E_s is in the range 7–15 eV/nm^2, which is comparable with the value we find by fitting the experiments. It can thus be concluded that surface free energies provide a sufficient driving force to cause dewetting *via* Si(001) surface diffusion.

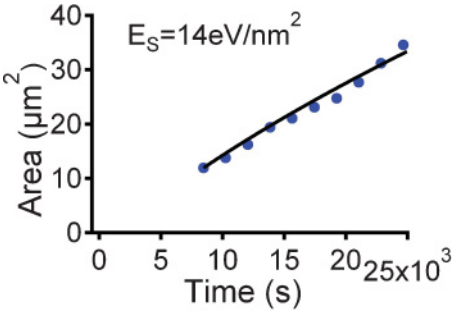

FIG. 4. (Color online) Area versus time measurements (dots) for a dewetting void at $T = 780$ °C in the initial regime where $A \propto t$. The solid line shows the best-fit solution obtained for a value of 14 eV/nm^2.

IV. RIM INSTABILITY AND SI FINGER FORMATION

As dewetting proceeds, square-shaped voids evolve and exhibit in turn a starlike shape as evidenced in Fig. 1(a). The time evolution of a given dewetting void area transits from a linear to a quadratic behavior [Fig. 1(b)]. This implies that the edges of the dewetting areas move on the average at a constant speed (i.e., $x \propto t$). The void edges, however, do not retract uniformly. Stroboscopic visualization (Fig. 5) illustrates the local variations of the void edge receding motion. Typically, two behaviors are observed. The dewetting front can locally slow down ($x \propto t^{1/2}$). At later times, these regions generate 3D structures, called in the following Si fingers, where mass is transferred and accumulated. Other regions of the dewetting front, called in the following void fingers (i.e., areas between two adjacent Si fingers), are characterized by a $x \propto t$ behavior. We refer to this as the steady-state regime where front moves at a constant average speed. The void fingers are responsible for the overall quadratic time evolution in time of the dewetted area, which is then characterized by the formation of periodic compact Si fingers interleaved with void fingers. The void fingers propagate most rapidly along ⟨100⟩ directions. As shown in Fig. 5 (white set squares), most void fingers exhibit a 90°-arrow end, suggesting that void fingers are terminated by {111} planes that intersect the {001} base plane along ⟨110⟩ directions. The void finger propagation, however, is constrained by impingement and nucleation of void fingers. This results in orientation of the Si fingers preferentially along ⟨100⟩ directions. {131} and {151} facets of Si fingers, however, may induce local bifurcations resulting in Si fingers oriented along ⟨130⟩ and ⟨150⟩ directions, which are the intersections of {131} and {151} planes with the {001} base plane (Fig. 9).

The 3D instability of the dewetting front has been theoretically studied by Kan and Wong in Ref. 20. The authors performed a 3D linear stability analysis of the dewetting front in the small-slope limit under a lateral x perturbation.

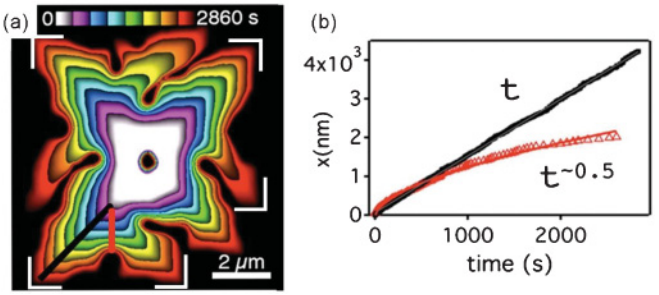

FIG. 5. (Color online) (a) Stroboscopic image of a dewetting area showing the local variations associated with the formation of Si and void fingers (SOI 14 ± 2 nm thick, $T = 800$ °C). The white set squares indicate the 90°-arrow termination of the void fingers. (b) Time evolution of the dewetting edge position along the two directions marked in (a) using lines with the corresponding color. Solid lines are least-squares fits to the data.

Numerical results show that (i) there is a coupling between the lateral x and vertical y instabilities. (ii) Fourier modes of the front response are characterized by a wave number k and a growth rate σ. The latter reaches a maximum for a critical wave number value, which is likely to correspond to the inter-Si finger distance observed in the steady-state dewetting regime (Fig. 9).

Figure 6 summarizes the temperature dependence of the experimental average inter-Si finger distance (λ_{fin}) and the wavelength characterized by the highest growth rate. The latter quantity is obtained from Ref. 20 using experimental front velocities as input for the $\sigma_m(b)$ curve, where b is proportional to the front velocity. Although developed in a small-slope approximation, Kan and Wong's model and the experimental data are in good qualitative agreement. A recent work[36] has raised a debate as to whether the observed 3D instability of the dewetting front should be attributed to a standard Rayleigh-Plateau instability or a diffusive kinetic instability. In the experiments, we have not been able to find evidence of a time dependence of the mode of largest amplitude nor the coarsening of the rim as predicted in Ref. 36.

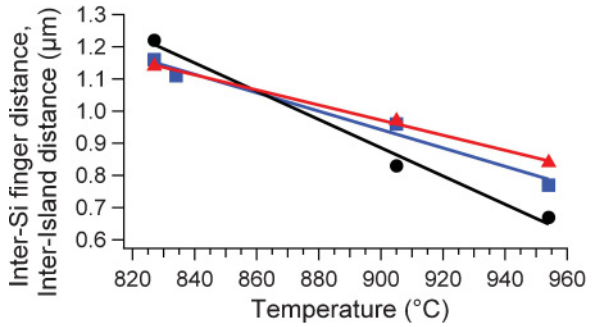

FIG. 6. (Color online) Temperature dependence of the interfinger distance (λ_{fin}) (black solid circles), the interfinger distance determined from Ref. 20 (red solid triangles), and the interisland distance (λ_{isl}) (blue solid squares). All quantities have been measured for 22-nm-thick films. Solid lines show the linear temperature dependence of λ_{fin} and λ_{isl}.

V. SI FINGERS AND DEWETTING ACTIVATION ENERGY

As described in the preceding section, once a dewetting front exhibits Si and void fingers, the void area evolves quadratically in time. In other words, the occurrence of fingers plays a major role in the overall dynamics.

To account for the 3D structure of the dewetting front exhibiting void fingers and Si fingers, we modify our 2D model described in Sec. III B. The simplified geometry of dewetting fronts with void fingers is defined in Fig. 7. In this approach, the thermodynamic driving force on the receding rim is only due to the *active* part of the rim, defined by the volume of effective length ζ and height h_m. The effective driving force acting on the length ζ reads as $F = -E_s\zeta$, and the mobility of a void finger characterized by a period λ_{fin} is $M = \Omega^2 D_s c/a^2 \lambda_{\text{fin}} h_m^2 w k_B T$. We thus obtain $v_{\text{front}} \approx v_{\text{rim}} \frac{\zeta}{\lambda_{\text{fin}}}$ with $h = h_m$. Assuming that the front velocity is thermally activated with an *effective* activation barrier E_{eff} (i.e., $v_{\text{front}} = Ce^{-E_{\text{eff}}/k_B T}$, where C is a constant term), we obtain a geometry-dependent activation barrier

$$E_{\text{eff}} = E_a + k_B T\,(\ln k_B T) + k_B T \ln\left(h_m^2 w \lambda_{\text{fin}}/\zeta\right), \quad (3)$$

where all quantities have been defined previously.

To confirm this approach, real-time LEEM measurements of the velocity of dewetting fronts exhibiting Si and void fingers have been done at different sample temperatures and for several initial film thicknesses [Fig. 8(a)]. Table II shows that the measured *effective* activation barrier (E_{eff}) depends on the initial Si-film thickness. Equation (3) also requires knowledge of the temperature evolution of the different geometrical parameters: λ_{fin}, h_m, w, and ζ. Figure 8(b) shows the temperature evolution of λ_{fin}, the only parameter that can be experimentally monitored.

Assuming that the temperature dependence of all the characteristic lengths (h_m, w, and ζ) scale as $\lambda_{\text{fin}}(T)$, we can estimate E_a by fitting numerically the curves shown in Fig. 8(a). In this numerical calculation, E_a and C are the only fit parameters as $\lambda_{\text{fin}}(T)$ is known [Fig. 8(b)]. The so-obtained fit curves are plotted as solid lines in Fig. 8(a) and numerical values of E_a are reported in Table II. For the different initial

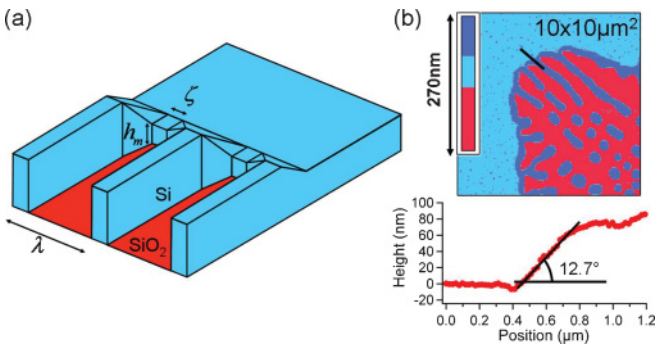

FIG. 7. (Color online) (a) Schematic of a receding front exhibiting fingers. Parameters ζ and h_m characterize the *active* part of the receding front. (b) AFM image of a dewetting area and the corresponding line profile illustrating the small-slope descending extremity of a Si finger (SOI 22 ± 2 nm thick, $T = 835$ °C).

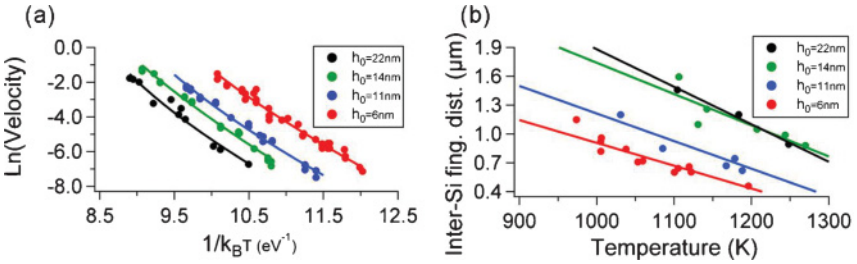

FIG. 8. (Color online) Temperature dependence (a) of the void growth velocity shown as an Arrhenius plot and (b) of the inter-Si finger distance measured for SOI films of various initial thicknesses. Solid lines are (a) corrected-Arrhenius fits (see text for details) and (b) linear fits.

Si thicknesses, a common value of the activation energy is found, $E_a = 2.0 \pm 0.2$ eV. This value is in good agreement with results reported in Ref. 21. In this study, the authors used optical methods to monitor, upon UHV annealing, the decay of a periodic structure patterned on a Si(001) surface and found an activation energy [identified to Si(001) surface self-diffusion] of $E_a = 2.3 \pm 0.1\,eV$. In both cases, despite the fact that different driving forces are at work (curvature-induced surface healing or dewetting), we expect Si diffusion to be kinetically limiting where mass is mainly agglomerated: in this study, at the descending extremity of the Si fingers shown in Fig. 7(b) (Si thin-film side). This small-slope region exhibits a high density of {001} terraces and should therefore favor Si accumulation by step flow. This result confirms *a posteriori* our scaling assumption as we obtain a common value of E_a despite initially a nonsimple Arrhenius law $[E_{\text{eff}}(h_0, T)]$.

VI. NANOISLAND FORMATION

In the steady-state regime, the void fingers govern the overall dynamics by shuttling mass from the triple line to the Si fingers, which lengthen and eventually break down into Si nanocrystals (Fig. 9). It has been widely reported that elongated solid structures, such as Si fingers, can agglomerate according to Rayleigh-Plateau instability.[15,16,37–39] Using surface-diffusion models, two quantities characterizing the island formation are derived. The interisland distance λ_{isl} results from energetics considerations: $\lambda_{\text{isl}} \propto h_{\text{Si}}$, from dimensional analysis. Considering a solid cylinder in the absence of a substrate, Nichols and Mullins[37] found $\lambda_{\text{isl}} = 2^{3/2}\pi r_0$, where r_0 is the cross-sectional radius. Including the contact angle θ_c between the elongated structure and the substrate, McCallum *et al.*[39] established $\lambda_{\text{isl}} = 2^{3/2}\pi r\sqrt{\frac{\theta_c - \sin\theta_c\cos\theta_c}{\theta_c \sin^2\theta_c}}$, where r is the projected half-width of the elongated structure ($r_0 = r/\sin\theta_c$). The characteristic time required between two island formation events in the case of a cylinder is $\tau_{\text{gen}} \propto r_0^4/B$, where B is the generalized diffusion coefficient introduced by Mullins.[40]

TABLE II. Effective activation energies E_{eff} calculated when assuming an Arrhenius behavior of the receding velocity of a dewetting front and estimated values of the activation energy E_a when using our expression of v_{fin} with the additional assumption that all the characteristic lengths scale as $\lambda_{\text{fin}}(T)$.

h_o (nm)	6 ± 2	11 ± 2	14 ± 2	22 ± 2
E_{eff} (eV)	2.7 ± 0.2	2.9 ± 0.2	3.1 ± 0.2	3.4 ± 0.2
E_a (eV)	1.9 ± 0.2	1.9 ± 0.2	2.2 ± 0.2	1.9 ± 0.2

Similarly, the growth rate of an instability of wavelength λ reads as $\sigma \propto B/r_0^4$.

Figure 10 compares our experimental results with preexisting theoretical predictions. Expressions for λ_{isl} found in Refs. 37 and 39 do not depend explicitly on temperature. However, as described in Sec. IV, the inter-Si finger distance decreases as the dewetting temperature is increased. Due to mass conservation, the geometrical parameter r (or r_0) is expected to behave as λ_{fin}. LEEM measurements show that $\lambda_{\text{isl}} \sim 6r$ while $2^{3/2}\pi \simeq 8.9$ and $2^{3/2}\pi\sqrt{\frac{\theta_c - \sin\theta_c\cos\theta_c}{\theta_c \sin^2\theta_c}} \simeq 8.2$ for $\theta_c = 73°$. Models based on Mullins approach for unsupported cylinders or elongated structures on a substrate seem to overestimate the interisland distance.

Using real-time LEEM measurements, we have been able to determine the average time between the generation of two subsequent Si nanocrystals from the same Si finger. The evolution of this characteristic time as a function of $1/B$ is shown in Fig. 10(b). The generalized surface-diffusion coefficient $B = \frac{D_s c \gamma_0 \Omega^2}{k_B T}$ (Ref. 40) has been calculated using the following values: Si surface-diffusion coefficient $D_s c = 10^{17}\, e^{\frac{-2.3eV}{k_b T}}$ nm^2/s,[21] Si surface energy density $\gamma_0 \sim 7$eV/nm^2, Si atomic volume $\Omega = \frac{1}{8}(0.5431)^3$ nm^3. From the slope of the $\tau_{\text{gen}}(1/B)$ curve and using a standard experimental value for r_0, we obtain $\tau_{\text{gen}} \sim 0.1\, r_0^4/B$. These results can be compared to numerical simulations obtained by McCallum *et al.*[39] and Dornel.[16] In the case of an infinite unsupported cylinder, Dornel showed that $(\tau_{\text{gen}})_{\text{inf}} \sim 30\, r_0^4/B$. McCallum *et al.*

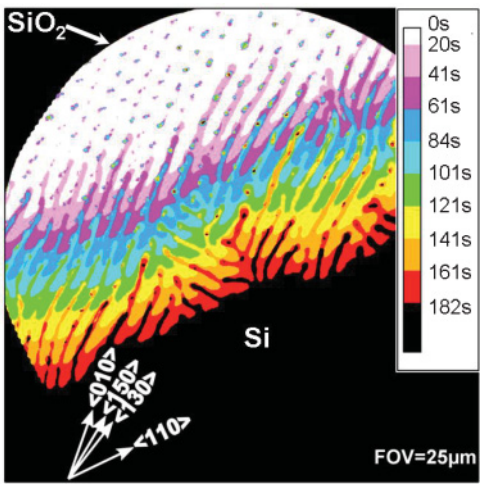

FIG. 9. (Color online) Stroboscopic image of the growth of a dewetting void showing the propagation of void fingers, a constant velocity, and the decomposition of Si fingers into Si nanoislands (SOI 22 ± 2 nm thick, $T = 975$ °C).

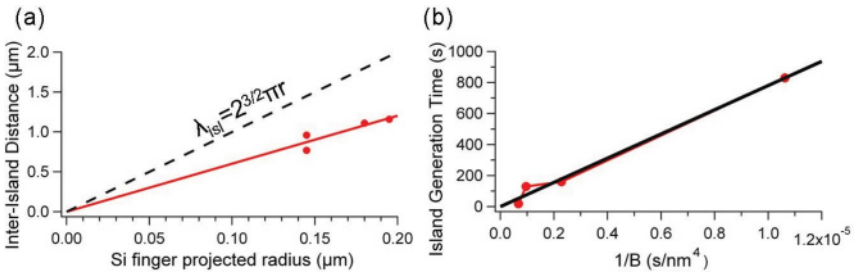

FIG. 10. (Color online) (a) Interisland distance λ_{isl} as a function the corresponding Si-finger projected half-width (r). (b) Average time between the generation of two adjacent Si nanocrystals from the same Si finger (τ_{gen}) as a function of $1/B$, where B is the generalized surface-diffusion coefficient introduced by Mullins (Ref. 40). Solid lines are linear fits.

included the contact angle between the unstable elongated structure and the substrate. By using the appropriate value of θ_c (in our case $\theta_c \sim 73°$), one can then determine that $(\tau_{gen})_{inf} \sim 24 r_0^4/B$. To the best of our knowledge, Ref. 16 is the only work to simulate the generation of individual Si nanostructures from the extremity of semi-infinite cylinders, as observed in experiments. In this study, Dornel obtained that for unsupported structures, $(\tau_{gen})_{semi} \sim 4.7\, r_0^4/B$. From these complementary results, it turns out that the effects of the substrate and an extremity accelerate the onset of instabilities. Again, standard models based on the Mullins approach, even when including the effect of the substrate, seem to underestimate the dynamic of the dewetting. Simulations of systems of finite size in contact with the substrate might be of high interest. One might also include the excess energy E_s in the local chemical potential as in our 2D model instead of considering only the local surface curvature.[19,36]

The structural properties of the Si nanoislands have been characterized during and after the completion of the dewetting process by grazing incidence x-ray diffraction (GIXD) and GISAXS (for a review, see Ref. 41).

Concerning the structure, we find that the Si-film crystallographic orientation is strictly preserved during the dewetting of the film [Fig. 11(a)] since no rotation of the Si nanoislands has been detected (in the limit of $\pm 0.5°$). All Si nanoislands exhibit the same facet orientation as confirmed by GISAXS. The GISAXS intensity scattered by the nanoislands has been measured over a three-dimensional volume of the reciprocal space. GISAXS patterns have been recorded at different azimuths, by rotating the sample by steps of 1° over a large angular range (100°). This complete set of GISAXS patterns shows 20 distinct scattering rods [Fig. 11(b)] arising from the facets of Si nanoislands. The largest are {113} and {111} facets and the smallest are {001} and {311}. They all belong to the Si equilibrium shape.[42] The occurrence of the {001} top facet is known from AFM data but is not measured accurately by GISAXS due to the predominance of the specular rod of the SiO_2 surface in the same region of reciprocal space. From these results, the facet size can be estimated from the full width at half maximum of the scattering rods. A schematic shape of Si nanoislands leading to the recorded GISAXS pattern is proposed in Fig. 11(c). Notice that for algorithmic reasons the reconstructed shape is assumed to be polyhedric, however, we can not exclude the existence of rounded parts as reported by Ref. 16.

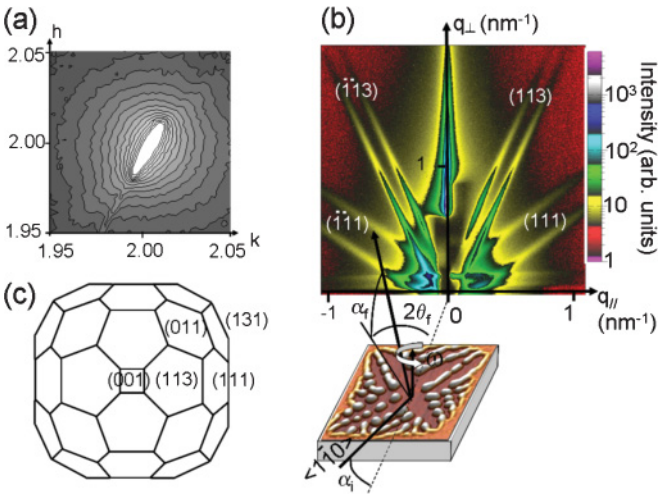

FIG. 11. (Color online) GIXD and GISAXS measurements after complete dewetting of a 22-nm-thick SOI film. (a) In-plane map of reciprocal space around (220) Bragg peak measured by GIXD. (b) Sketch of the GISAXS geometry and pattern measured with the incident beam aligned in the ⟨1-10⟩ direction. Extended scattering rods from {113} and {111} facets are observed. (c) Mean shape of Si nanoislands extracted from the analysis of GISAXS patterns.

VII. POTENTIAL ADDITIONAL EFFECTS

As shown in this paper and in Ref. 19, SOI dewetting is mainly driven by surface-free-energy minimization and mediated by surface diffusion. However, some other phenomena could also influence SOI dewetting such as Si-SiO_2 chemical reaction, stress, and shape effects.

(1) *Chemical reaction effect on the dewetting rate.* In our experimental conditions ($P < 10^{-9}$ Torr and $T < 1000$ °C), the silicon and the buried oxide react.[43] As the SiO_2 is exposed, the SiO_2+2Si→2SiO reaction occurs. From an estimation of the oxide decomposition rates reported in Ref. 22, the activation energy for oxide decomposition is around 4.1 eV while we measure a dewetting activation energy $\simeq 2.0 \pm 0.2$ eV (Sec. V). The chemical reaction thus does not consume a significant amount of Si during dewetting. More precisely, we estimate that in our experimental conditions, ∼1% of the Si film is lost during the chemical reaction, which is consistent with the depth of the grooves observed in the remaining SiO_2 after Si agglomeration.

(2) *Stress effects.* The process of fabrication of our sample (Smart Cut© process) leads to single-crystalline Si films without any grain boundaries that could cause local stresses. Furthermore, thanks to its lateral dimensions as well as its thickness, intrinsic surface-stress can not induce any bulk stress in the film.[44,45] We have checked by x-ray

diffraction at the European Synchrotron Radiation Facility (ESRF) that the samples are strain free. However, from a more general point of view, we can wonder about stress effects on the SOI dewetting process. For this purpose, we have measured the dewetting rates of SOI films biaxially strained (1% of strain). The dewetting rates we found are the same (within experimental uncertainties) for both strained and unstrained materials. This is expected since the driving force for SOI dewetting ($E_s \sim 14\text{eV/nm}^2$) is very large compared to the elastic energy, which for a strain of 1% is only $\sim 0.1 E_s$.[46]

(3) *Shape effects.* Our geometrical assumptions for the rim shape enable us to give simple analytic expressions of the dewetting velocities based on surface diffusion on the {001} facet of the rim. However, in the experiments, the rim exhibits additional facets (e.g., {311}, {111} facets) that may play a role in the Si diffusion *via*, for instance, their surface energies and/or surface-diffusion properties. In our temperature range, the surface energy anisotropy is less than 10%,[35,42] so that its influence on the amplitude of the dewetting driving force ($\sim E_s$) is not expected to be significant. Also, Watanabe *et al.*[47] have pointed out that the self-diffusion on {110} and {111} facets are all similar to that of the Si(001) surface. This implies that the occurrence of additional facets should not influence the mobility (M) of the dewetting front. Finally, our expression of the driving force neglects the contribution of the shape change. Whatever the true shape of the profile is, the driving force can always be divided into a contribution due to the shift of the rim at constant shape ($\sim E_s$) and a contribution due to the shape modification of the rim at constant position. This second contribution can be neglected because of the high value of E_s we find for the SOI system. We could imagine opposite situations for which the driving force essentially originates from the shape modification of the rim. This may be the case for systems in which the dewetting is not driven by surface energy, but only by elastic relaxation.[46]

VIII. SUMMARY

Using the LEEM microscopy technique as a powerful method for studying *in situ* and in *real-time* the surface dynamics of SOI dewetting, we conclude that (i) the dewetting dynamics as well as the dewetted morphologies are extremely sensitive to the sample preparation. (ii) The early-stage void opening (Area $\propto t$) is accompanied by a layer-by-layer rim thickening. A 2D analytic model, described and discussed with respect to the previous reports, is used to determine a SOI dewetting driving force of $E_s \sim 14$ eV. (iii) The observed 3D rim instability is not inconsistent with a standard Rayleigh-Plateau interpretation. (iv) In the long-time limit (Area $\propto t^2$), a Si(001) surface self-diffusion energy $E_a = 2.0 \pm 0.2$ eV is determined, using a 3D analytic model, in good agreement with the values obtained from the literature. This suggests that the dewetting is kinetically limited by Si diffusion where mass is mainly accumulated: at the descending extremity of the Si fingers resulting from the 3D rim instability. (v) The Si fingers create individual Si islands. The measured dynamics can not solely be explained by standard stability analysis; based on Mullins diffusion equation, finite-size effects are expected to play a significant role. (vi) The resulting nanoislands exhibit {113}, {111}, {011}, and {311} facets, expected for the Si equilibrium shape.

ACKNOWLEDGMENTS

This work was supported by ANR grant PNANO DéFIS (Grant No. ANR 08-nano-036) and by APO grant delivered by Provence Alpes Côte d'Azur Region Council. The authors would like to thank J. Eymery and N. Blanc for fruitful discussions and their help during our beamtime access at the ESRF. Beamline BM32 staff are also acknowledged. The authors thank A. Locatelli for allowing preliminary studies on the beamline *nanospectroscopy* at the synchrotron *Elettra* (Trieste, Italy).

*cheynis@cinam.univ-mrs.fr

†Permanent address: Photonic Microsystem Technologies, Sandia National Labs, PO Box 5800, Albuquerque, NM.

[1] E. Jiran and C. V. Thompson, J. Electron. Mater. **19**, 1153 (1990).

[2] C. Schrank, C. Eisenmenger-Sittner, E. Neubauer, H. Bangert, and A. Bergauer, Thin Solid Films **459**, 276 (2004).

[3] K. Thurmer and N. C. Bartelt, Phys. Rev. Lett. **100**, 186101 (2008).

[4] K. F. McCarty, J. C. Hamilton, Y. Sato, A. Saá, R. Stumpf, J. de la Figuera, K. Thurmer, F. Jones, A. K. Schmid, A. A. Talin, and N. C. Bartelt, New J. Phys. **11**, 043001 (2009).

[5] J. Ye and C. V. Thompson, Appl. Phys. Lett. **97**, 071904 (2010).

[6] Y. Ono, M. Nagase, M. Tabe, and Y. Takahashi, Jpn. J. Appl. Phys. **34**, 1728 (1995).

[7] R. Nuryadi, Y. Ishikawa, and M. Tabe, Appl. Surf. Sci. **159-160**, 121 (2000).

[8] B. Legrand, V. Agache, J. P. Nys, V. Senez, and D. Stiévenard, Appl. Phys. Lett. **76**, 3271 (2000).

[9] B. Legrand, V. Agache, T. Mélin, J. P. Nys, V. Senez, and D. Stiévenard, J. Appl. Phys. **91**, 106 (2002).

[10] R. Nuryadi, Y. Ishikawa, Y. Ono, and M. Tabe, J. Vac. Sci. Technol. B **20**, 167 (2002).

[11] B. Yang, P. Zhang, D. E. Savage, M. G. Lagally, G. H. Lu, M. Huang, and F. Liu, Phys. Rev. B **72**, 235413 (2005).

[12] E. Sutter and P. Sutter, Nanotechnology **17**, 3724 (2006).

[13] D. T. Danielson, D. K. Sparacin, J. Michel, and L. C. Kimerling, J. Appl. Phys. **100**, 083507 (2006).

[14] E. Dornel, J.-C. Barbé, F. de Crécy, G. Lacolle, and J. Eymery, Phys. Rev. B **73**, 115427 (2006).

[15] D. T. Danielson, Ph.D. thesis, MIT, 2008.

[16] E. Dornell, Ph.D. thesis, UJF, Grenoble, 2007.

[17] Y. Fan, R. Nuryadi, Z. A. Burhanudin, and M. Tabe, Jpn. J. Appl. Phys. **47**, 1461 (2008).

[18] Z. A. Burhanudin, R. Nuryadi, Y. Ishikawa, M. Tabe, and Y. Ono, Appl. Phys. Lett. **87**, 121905 (2005).

[19] E. Bussmann, F. Cheynis, F. Leroy, P. Müller, and O. Pierre-Louis, New J. Phys. **13**, 043017 (2011).

[20]W. Kan and H. Wong, J. Appl. Phys. **97**, 043515 (2005).
[21]M. E. Keefe, C. C. Umbach, and J. M. Blakely, J. Phys. Chem. Solids **55**, 965 (1994).
[22]H. Hibino, M. Uematsu, and Y. Watanabe, J. Appl. Phys. **100**, 113519 (2006).
[23]R. Miotto and A. Ferraz, Surf. Sci. **603**, 1229 (2009).
[24]G. Capellini, G. Giasca, M. de Seta, A. Notargiamoco, F. Evangestelli, and M. Nardonne, J. Appl. Phys. **105**, 093525 (2009).
[25]O. Pierre-Louis, A. Chame, and Y. Saito, Phys. Rev. Lett. **103**, 195501 (2009).
[26]A. K. Schmid, N. C. Bartelt, and R. Q. Hwang, Science **290**, 1561 (2000).
[27]K. Morgenstern, G. Rosenfeld, B. Poelsema, and G. Comsa, Phys. Rev. Lett. **74**, 2058 (1995).
[28]O. Pierre-Louis, A. Chame, and M. Dufay, Eur. Phys. J. B **77**, 57 (2010).
[29]R. Brandon and F. J. Bradshaw, Royal Aircraft Establishment Report No. 66095.
[30]H. Wong, P. Voorhees, M. Miksis, and S. Davis, Acta Mater. **48**, 1719 (2000).
[31]D. J. Srolovitz and S. Safran, J. Appl. Phys. **60**, 255 (1986).
[32]R. Jaccodine, J. Electrochem. Soc. **110**, 524 (1963).
[33]D. J. Eaglesham, A. E. White, L. C. Feldman, N. Moriya, and D. C. Jacobson, Phys. Rev. Lett. **70**, 1643 (1993).
[34]J.-J. Métois and P. Müller, Surf. Sci. **548**, 13 (2004).
[35]P. Müller and J.-J. Métois, Thin Solid Films **517**, 65 (2008).
[36]M. Dufay and O. Pierre-Louis, Phys. Rev. Lett. **106**, 105506 (2011).
[37]F. A. Nichols and W. W. Mullins, Trans. AIME **233**, 1840 (1965).
[38]D. J. Srolovitz and C. V. Thompson, Thin Solid Films **139**, 133 (1986).
[39]M. McCallum, P. Voorhees, M. Miksis, S. Davis, and H. Wong, J. Appl. Phys. **79**, 7604 (1996).
[40]W. W. Mullins, J. Appl. Phys. **28**, 333 (1957).
[41]G. Renaud, R. Lazzari, and F. Leroy, Surf. Sci. Rep. **64**, 255 (2009).
[42]J.-M. Bermond, J.-J. Métois, X. Egea, and F. Floret, Surf. Sci. **330**, 48 (1993).
[43]K. Sudoh and M. Naito, J. Appl. Phys. **108**, 083520 (2010).
[44]R. Kern and P. Müller, Surf. Sci. **392**, 103 (1997).
[45]P. Müller, P. Turban, L. Lapena, and S. Andrieu, Surf. Sci. **488**, 52 (2001).
[46]F. Cheynis, E. Bussmann, F. Leroy, T. Passanante, and P. Müller, Int. J. Nanotechnol. **8** (2011), (in press).
[47]F. Watanabe, S. Kodambaka, W. Swiech, J. Greene, and D. Cahill, Surf. Sci. **572**, 425 (2004).